One-Pot Synthesis of Zinc Oxide Nanoparticle for Bromophenol Blue Adsorption and Its Antifungal Activity Against Filamentous Fungi

Kovo Akpomie (kovo.akpomie@unn.edu.ng)
University of the Free State
Soumya Ghosh
University of the Free State
Marieka Gryzenhout
University of the Free State
Jeanet Conradie
University of the Free State

Research Article

Keywords: Synthesis, dye adsorption, filamentous fungi, antifungal, nanoparticle, zinc oxide

Posted Date: December 9th, 2020

DOI: https://doi.org/10.21203/rs.3.rs-116179/v1

Version of Record: A version of this preprint was published at Scientific Reports on April 15th, 2021. See the published version at https://doi.org/10.1038/s41598-021-87819-2.

Abstract

Zinc oxide nanoparticles (ZnONP) have gained attention in recent years due to their multifunctional uses, potent adsorptive potential and effective antifungal activities. Despite these desirable characteristics, ZnONP has not been used for the adsorption of bromophenol blue (BRB) and tests as antifungal agents against certain important filamentous fungal strains have been limited. In this research, ZnONP was prepared via a facile one-pot synthetic approach and applied in the adsorption of BRB and as an antifungal agent against the filamentous fungi and plant pathogens; *Alternaria alternata* CGJM3078, *Alternaria alternata* CGJM3006 and *Fusarium verticilliodes* CGJM3823. The ZnONP was characterized by the UV, FTIR, XRD, TGA, BET, SEM, TEM, and EDX techniques, which showed efficient synthesis. The characteristics ZnO UV absorption band was observed at 375 nm, while the XRD showed an average ZnONP crystalline size of 47.2 nm. The SEM and TEM images showed an irregular shaped and aggregated porous structure of 65.3 nm average-sized ZnONPs. The Freundlich, pseudo-second-order, and intra-particle diffusion models showed $R^2 > 0.9494$ and SSE < 0.7412, thus, exhibited the best fit to the isotherm and kinetics of adsorption. Adsorption thermodynamics revealed feasible, endothermic, random, and spontaneous adsorption of BRB onto the synthesized ZnONPs. The antifungal assay conducted, depicted strong antifungal activities against all three tested fungal cultures. A model was proposed on what causes this antifungal effect. This research demonstrated the potent use of ZnONP for the adsorption of BRB and as effective antifungal agents.

Introduction

In recent years, there have been growing concerns arising from the rapid pollution of water bodies around the world [1]. This is attributed to technological advancements resulting in the rapid growth of industries, and subsequently the pollution of water from industrial effluents [2]. Again, agricultural pesticides, fertilizers, and herbicides are easily washed off by running water into receiving water bodies [3]. This water pollution has significantly affected aquatic lives, made the water unsafe for drinking, and resulted in several health effects [4,5]. Among several water pollutants, dyes have gained significant attention from environmental scientists [6]. This is because dyes are extensively used in the textile, leather, cosmetic, and paper industries [7]. The textile industry alone consumes over 700,000 tons of dyes annually [8,9]. Thus, there is a high amount of dyes in the effluents released from these industries. Apart from that, dyes are allergenic, mutagenic, and carcinogenic at certain concentrations, hazardous, affect photosynthesis in marine organisms, and are resistant to biodegradation [10]. Therefore, the treatment of dye-polluted water is important.

Bromophenol blue (BRB) dye is widely used as a laboratory indicator and in the textile and printing industries [8,11]. However, most studies have focused on the treatment of water contaminated with dyes such as methylene blue, congo red, and malachite green, but only a few studies are documented the removal of BRB despite its harmful nature in the environment [12]. Hence, this research considers the removal of BRB from water.

Several methods have been utilized over the years for the treatment of dye-polluted water such as filtration, coagulation, solvent extraction, precipitation, adsorption, ion exchange, floatation, biological treatment, catalytic degradation, ozonation, and oxidation [13,14]. Adsorption is the most efficient and promising method but is limited by the high cost of activated carbon used as a commercial adsorbent for water treatment [9,15]. Therefore, other efficient low-cost adsorbents such as bio-waste, natural inorganic materials, polymeric materials, and nanomaterials have been harnessed as suitable alternatives to activated carbon [10,16–21].

Among the alternative adsorbents, nanomaterials have gained tremendous attention in recent years due to their high efficiency, high surface reactivity, broad application for several purposes, and environmental compatibility [8,17,22].

Metallic nanoparticles are known to be promising owing to their efficient adsorptive and catalytic degradation potentials for dye containing water [23–25]. In particular, zinc oxide nanoparticle (ZnONP) has received significant attention for water treatment because of its nontoxicity, long-term stability, acceptable cost, biocompatibility, and potent antimicrobial activities against microbes frequently encountered in water [26,27]. Thus, a combination of the adsorption potentials and the antimicrobial activities in water treatment would be highly effective to obtain portable water. Therefore, the efficient treatment of dye-polluted water by the use of ZnONPs is well documented [26,28,29]. However, from a thorough literature search, there is no evidence of the use of ZnONP in the adsorption of BRB from water. Thus, this study evaluated the potentials of ZnONP for the treatment of BRB polluted water.

Several studies have been performed on the antibacterial and antifungal activities of ZnONPs, which proved that ZnONP is a potent antimicrobial agent [27,30–33]. However, studies on the antifungal activity of nanoparticles against filamentous fungi are rare [34,35]. In this study the two plant pathogens were studied. The filamentous fungus *Alternaria alternata* is a pathogen of fruit and vegetables such as strawberries, tangerines, mandarins, grapefruits, and tomatoes, thus causing extensive post-harvest spoilage and loss [36]. The pathogenicity of *A. alternata* is due to their secretions of host-selective toxins (HST) such as Alternaria alternariol (AAL)-toxin and Alternaria F (AF)-toxin [37]. Additionally, *A. alternata* employs cell wall degrading enzymes, such as pectic enzymes, and organic acids [36] that lower the pH and act synergistically with the enzymes to digest Calsium-acetate, which causes damage to the host tissues [36]. In humans, *Alternariaalternata* are/is associated with hypersensitivity pneumonitis, bronchial asthma, allergic sinusitis, rhinitis, and cutaneous, subcutaneous infections in humans [38].

The filamentous fungus *Fusarium verticilliodes* is a seed-borne endophytic pathogen of maize and cereals such as wheat, and can infect a wide variety of other plants worldwide [39]. This fungus is the causative agent for ear rot, kernel rot and seedling blight of maize, and head blight of wheat and therefore largely responsible for pre- and post harvest losses [40]. For humans and animals *F. verticilliodes* secretes fumonisin B that accumulates in the kernels of maize or wheat, causing toxicity in resulting food commodities [41]. Fumonisin B1 toxin causes nephrotoxic, hepatotxic and cytotoxic effects on the livestock cattle such as lambs [42]. Besides fumonisin, infected seeds in storage conditions are capable of producing moniliformin, zearoleanone and trichothecene that cause up to 20% grain loss [43] and that also represent dangerous mycotoxins [42]. *Fusarium* mycotoxin adulteration in agricultural commodities poses a global threat to food safety and has substantial economic significances. *F. verticilliodes* outbreaks have been reported in many countries in Asia, New Zealand, Africa, Europe, and South America [44]. For example, in the USA an economic model study showed a significant loss (US$ 31–46 million) of animal feed grains in a year with a *F. verticilliodes* outbreak in comparison to a normal year (non-significant *F. verticilliodes* infection), where losses were merely US$ 1–20 million [45].

There is a need to discover novel control agents to prevent plant diseases and post-harvest losses of food crops and grains associated with filamentous fungi, as well as to minimize harmful effects of these fungi on humans and livestock. Although a few studies have reported ZnONP antifungal activities against *Alternaria alternata* [34,35], no study was conducted specifically on these two South African strains (CGJM3078 and CGJM3006) of *Alternaria alternata*. No antifungal studies with ZnONP were conducted so far against strains of *F.verticilliodes*. The present study investigated the extent of the antifungal activities of ZnONP against these economically significant postharvest fungal pathogens, especially with the particular ZnONP particles developed in this study.

The aim of this study is the evaluation of the adsorptive potentials of ZnONP for BRB dye as well as its antifungal activity against *A. alternata* and *F. verticilliodes*. The ZnONP was synthesized by a simple traditional one-pot

chemical reduction approach and characterized. The synthesized ZnONP was utilized for BRB adsorption at changing pH, dye concentration, material dosage, temperature, and time. The thermodynamics, kinetics, and isotherm of the adsorption process were evaluated for a proper understanding of the dye adsorption process. Finally, the antifungal activity of the synthesized ZnONP against *A. alternata* and *F. verticilliodes* was investigated *in-vitro*, and a possible mechanism of action against these fungi is proposed.

Materials And Methods

Chemicals used

Zinc acetate dihydrate ($Zn(CH_3COO)_2.2H_2O$), bromophenol blue ($C_{19}H_{10}Br_4O_5S$), sodium hydroxide (NaOH), nitric acid (HNO_3), and hydrochloric acid (HCl) were purchased from Sigma-Aldrich, South Africa. All the chemicals were used as purchased without any purification.

Synthesis of ZnONP

A simple one-pot synthesis via chemical reduction was utilized for the preparation of ZnONP [46]. Herein, 4.0 g of zinc acetate was added to 100 mL of distilled water in a beaker. The solution was stirred with a magnetic stirrer on a hot plate at 30 ^oC for 40 min. This was followed by the dropwise addition of 0.2 M NaOH to the solution with continuous stirring until the pH was 11.0. The solution became white due to the precipitation of ZnO and was stirred further for 1 h, after which it was allowed to stand for 50 min. The filtrate was decanted and the synthesized ZnONP was washed repeatedly with excess distilled water until neutral pH and finally with ethanol. The prepared ZnONP was dried in an oven at 250 ^oC for 5 h. The as-prepared nano-sorbent was stored in an airtight sample container and kept in a desiccator until use.

Characterization of the synthesized ZnONP

The ZnONP was characterized to evaluate the surface properties necessary for efficient adsorption of BRB from water. The field emission scanning electron microscopy (FE-SEM; Jeol model) was used to examine the particle size and morphology, while the Energy-dispersive X-ray spectroscopy (EDS; Oxford model) coupled to the SEM instrument was used to determine the elemental composition. The morphology and surface structure was further analyzed with the Transmission electron microscopy (TEM) (Philips-FEI-CM100 model) equipped with a Mega View III digital camera. The functional groups of ZnONP were examined by the Fourier transform infrared (FTIR) spectroscopy (FTIR; Bruker Tensor 27 model). The crystalline phases were identified by the X-ray diffractometer (XRD; Brucker model) with Cu radiation of 1.5 Å at the 2-theta range of 10 – 80^o. The pH drift method was used to evaluate the pH point of zero charge (pHpzc) as described elsewhere [47]. The absorption spectrum of the ZnONP was obtained using distilled water as a reference with the UV-Spectrophotometer (Shimadzu UV-1800 model) in the range 250 to 850 nm. Thermal stability was analyzed by the thermo-gravimetric analyzer (TGA; Mettler Toledo Model). The surface area analyzer (Micrometrics ASAP 2020 model) was used to examine the Surface area (S_{BET}) and pore properties and the results were refined by the MicroActive VI.01 software.

Table 1: Effect of various parameters and operating conditions on the adsorption of bromophenol blue onto ZnONPs

Parameters	Range studied	Conditions maintained
Solution pH	2, 3, 4, 5, 6, 7, 8, 9	Dosage 0.1 g, dye conc 50 mg/L, time 180 min, temp 300 K.
ZnONP dosage (g)	0.1, 0.15, 0.2, 0.25, 0.3	pH 4.0, dye conc 50 mg/L, time 180 min, temp 300 K.
Dye concentration (mg/L)	10, 20, 30, 40, 50	pH 4.0, dosage 0.1 g, time 180 min, temp 300 K.
Sonication time (min)	5, 10, 20, 40, 60, 80, 100, 120, 140, 160, 180	pH 4.0, dosage 0.1 g, dye conc 50 mg/L, temp 300 K.
Temperature (K)	300, 306, 313, 318, 323	pH 4.0, dosage 0.1 g, dye conc 50 mg/L, time 180 min.

Adsorption removal

A stock solution of BRB was made by dissolving 50 mg of $C_{19}H_{10}Br_4O_5S$ in a 500 mL volumetric flask to make a concentration of 100 mg/L. Serial dilution of the stock was done to obtain lower concentrations of 10 – 50 mg/L. The pH of the solution was adjusted from 2.0 to 9.0 using 0.1 M NaOH and HCl. Batch adsorption was applied to determine the influence of solution pH, ZnONP dosage, BRB concentration, sonication time, and temperature at the operating conditions presented in **Table 1**. Batch BRB adsorption was carried out by adding a given amount of ZnONP to 10 mL of a given BRB concentration at the specified pH. The mixture was sonicated at a particular temperature in an ultrasonic 2.5 L water-filled bath at the specified time. At the end of the given time, the solution was centrifuged at 8000 rpm for 30 min, and the filtrate was analyzed for residual BRB at a maximum wavelength of 590 nm, using the UV Spectrophotometer (Shimadzu UV-1800 model). The percentage adsorption and uptake capacity q_e (mg/g) were calculated from the percentage removal and mass balance equations, respectively [8]:

$$Adsorption\ (\%) = \left(\frac{(C_o - C_e)}{C_o}\right) * 100 \quad (1)$$

$$q_e = \frac{(C_o - C_e)V}{m} \quad (2)$$

Where C_e and C_o in mg/L are the final and initial concentrations of BRB in solution, respectively. m (g) is the mass of ZnONP used and V (L) is the volume of BRB solution used.

Isotherm, kinetic and thermodynamics of adsorption

The isotherm modeling on the adsorption of BRB onto ZnONP was evaluated from the Freundlich, Temkin, Langmuir, and Flory-Huggins models [12]. The adsorption kinetics was deduced from the pseudo-first-order (PFO), pseudo-second-order (PSO), liquid film diffusion (LFD), and intraparticle diffusion (IPD) rate models, while thermodynamics was deduced from Van't Hoff's equation [48]. The equation and symbols of the isotherm, kinetics, and thermodynamics are described in the supplementary information.

Statistical analysis

Each experiment was done in duplicate and the average value was computed. The error bars in the figures indicate the standard deviation from the mean. The statistical function of the origin 2019b software was used to determine the sum square error (SSE) and the coefficient of determination (R^2), used to analyze the best-fitted isotherm or kinetic model.

Antifungal analysis

The *in-vitro* antimicrobial activities of the ZnONP were tested against the three fungal strains, *viz A. alternata* CGJM3078, *A. alternata* CGJM3006, and *F verticilliodes* CGJM3823 fungi [CGJM= Cultures Gert Johannes Marais]. The fungal strains were procured from Dr. Gert Marais, Department of Plant Sciences, University of the Free State, Bloemfontein, South Africa. The antimicrobial activity screening was performed with the well diffusion technique [49,50] on malt agar (Malt extract 2%; Dextrose 2%; Agar 2% Biolab, Merck, Johannesburg) media plates. For the technique, a pinch amount of mycelia scraping from each of the fungi was inoculated in 15 mL of Malt extract dextrose broth (Malt extract 2%; Dextrose 2%) and cultivated for 3 days at 25 °C. Following the incubation, the cultures were adjusted to a concentration of 10^6 cfu/mL (cfu – colony forming units), inoculated in molten Malt Extract Agar, swirled gently, and poured into 90 mm Petri plates (Ascendis, Johannesburg). The inoculated plates were dried under a Bio-Safety Cabinet Class II (ESCO Technologies Pty Ltd, Gauteng, South Africa).

Following air-drying, the solidified agar media plates were bored (bore size = 5 mm) with wells with a metallic plug borer and filled with 40 µL of the ZnONP made into 2-fold serial dilutions (0.002, 0.004, 0.009, 0.019, 0.039, 0.078, 0.156, 0.312, 0.625, 1.25, 2.5, 5) mg/mL, in accordance to a previous study [32]. Bleach disinfectant [$Ca(ClO)_2$] (5%) served as the positive control while sterile distilled water was used as the negative control for all the experiments. Plates were incubated at room temperature in the upright position until zones of inhibition were observed, which was considered an endpoint parameter for the antimicrobial activities. The diameter of the inhibition zones was measured using the Image J software program (https://imagej.nih.gov/ij/) as per a previous study [50]. All the culture media were procured from Sigma Aldrich, Merck KGaA, Darmstadt, Germany, and Neogen Culture media, Heywood, UK respectively.

Results And Discussion

Characterization of ZnONP

The XRD characterization used to examine the crystalline phases of ZnONP is shown in **Fig. 1a.** The spectrum showed diffractions patterns at 2θ values of 31.69°, 34.33°, 36.11°, 47.43°, 56.49°, 62.76°, 66.23°, 67.88°, 68.97°, 72.37° and 76.93°, which conforms to the hexagonal ZnO crystalline planes of (100), (002), (101), (102), (110), (103), (200), (112), (201), (004) and (202) respectively, as indexed in the standard JCPDS card no. 36-1451 [26]. This confirms the successful synthesis of ZnO. In addition, the as-prepared ZnONP had a high crystalline structure as revealed by the high intensity of the diffraction peaks. Apart from that, the fact that no other diffraction peak was observed in the XRD suggests pure synthesized ZnONP. The average nanoparticle crystalline size of ZnONP as deduced from the Debye-Scherrer's equation was 47.2 nm using the characteristic peak at 36.11°. This size was larger than 15.41 nm and 5 – 15 nm reported from the green synthesis of ZnONPs using aqueous extracts of *Deverra tortuosa* [51] and *Mussaenda frondsa* [52] respectively.

The FTIR spectra of ZnONP before and after the adsorption of BRB is shown in **Fig. 1b**. The spectra help to identify the functional groups present on ZnONP. The band at 3369 cm^{-1} corresponds to the O-H stretching vibration, while

the O=C=O functionality of absorbed CO_2 on the ZnONP was depicted by the bands at 2162 cm^{-1} and 2008 cm^{-1} [53]. The absorption band at 1380 cm^{-1} corresponds to the OH bending of water acquire from the absorption of moisture from air [26]. Also, the Zn-O stretching vibrations were indicated by the bands at 887 cm^{-1} and 550 cm^{-1}, which confirms the successful synthesis of the ZnONP. After the adsorption of dye, the BRB-loaded ZnONP showed shifts in absorption bands from 3369 to 3377 cm^{-1} and 1380 to 1330 cm^{-1} for OH, from 2008 to 2033 cm^{-1} for the O=C=O, and from 550 to 557 cm^{-1} for the Zn-O functionalities. This indicated the involvement of the OH and Zn-O groups in the uptake of BRB on the adsorbent and that the mechanism of BRB uptake on ZnONP could be attributed to electrostatic interactions, H-bonding as well as weak Vander Waals interaction [46].

The UV spectrum of the as-prepared ZnONP is shown in **Fig. 1c**. The characteristic ZnO peak was observed at 375 nm, this corroborates the efficient and successful synthesis of ZnONP. The absorption at 375 nm is attributed to the intrinsic bandgap of ZnO from the valence to the conduction bands resulting from the electronic transitions [54]. Similar UV absorption was achieved at 374 nm for the green synthesis of ZnONP using the aqueous extract of *Deverra tortuosa*. The thermal stability of the synthesized ZnONP was evaluated from the TGA as presented in **Fig. 1d.** Significant weight loss was observed from 98 to 206 ^oC, which could be attributed to the removal of absorbed water, CO_2 as well as other low-temperature components from the synthesized ZnONP. At 800 ^oC, the ZnONP showed a weight loss of 22.92% indicating high thermal stability of 78.98%. The as-prepared ZnONP demonstrated efficient thermal stability in comparison to that prepared by Yuvaraja et al [28], which showed over 35% weight loss up to 450 ^oC. This indicated the efficiency of our synthetic procedure in the preparation of ZnONP with enhanced thermal characteristics for higher temperature applications.

The nitrogen adsorption-desorption isotherm **(Fig. 1e)** of the ZnONP as obtained from BET analysis revealed a surface area of 9.259 m^2/g and correlated with type III isotherm according to the IUPAC classification [46]. Also, the pore characteristics (**Fig. 1f**) as obtained from the Barret-Joyner-Halenda (BJH) method showed a pore volume of 0.037453 cm^3/g and an average pore diameter of 9.87 nm indicating the mesoporous structure. Although the surface area of our as-prepared adsorbent was, lower than 26.78 m^2/g obtained from the hydrothermal synthesis of ZnONP used in the adsorption of heavy metals [26], the mesoporous structure (see discussion in the next paragraph) would be highly influential for the efficient removal of dye molecules from solution [55].

The SEM images of the as-prepared ZnONP are shown in **Fig. 2a** and **Fig. 2b**. As observed, the ZnONP adsorbent is associated with an irregular surface structure, particle aggregation, with a highly porous morphology, which corroborates the porosity measurements. The average ZnONP size of 65.3 nm was obtained from the SEM structure. Again, the porous structure of the synthesized ZnONP would ensure easy diffusion of dyes molecules favoring efficient adsorption of the pollutant from solution [56]. The agglomerated characteristics of the synthesized ZnONP was further verified from the TEM image (**Fig. 2c**). Besides, the EDX spectra (**Fig. 2d**) of the adsorbent, showed 78.9% zinc and 21.1% oxygen, which further confirms the successful synthesis of the ZnONP. The absence of other elements also indicates a pure synthesized ZnONP, which corroborates the results of the XRD analysis. A similar finding was also reported by other workers [26,57,58]. The absence of impurities in the synthesized ZnONP is important for efficient antimicrobial activity [58].

BRB uptake on ZnONP

Several operating parameters such as the temperature of the solution, dye concentration, solution pH, time, and material dosage are known to influence the overall uptake of pollutants onto adsorbent materials [17,59,60]. Thus, we

investigated the effect of these parameters on the uptake of BRB onto ZnONP. **Fig. 3a** illustrates the influence of pH on dye removal from solution onto the as-prepared particle. A steady decrease in the adsorbent's adsorption capacity and percentage uptake of BRB from pH 2.0 to 6.0 was obtained after which a slight increase up to pH 9.0 was observed. This trend is strongly dependent on the pHpzc of ZnONP as well as the pKa of BRB dye in solution. The pHpzc of the synthesized ZnONP was 6.3 while BRB has a pKa value of 3.84 [8]. Thus, ZnONP is associated with a positive surface charge at pH values below 6.3 but becomes negative above this pH. Also, BRB exists as negatively charged molecules below 3.84 after which it becomes neutral and then exists as positively charged species as pH increases. Thus the optimum uptake achieved at pH values below 4.0 was due to strong electrostatic attraction between the positive ZnONP surface and the anionic BRB species in solution. Again, the slight increase observed from pH 6.0 to 9.0 is probably due to the attraction between positively charged BRB species in solution and the negatively charged adsorbent surface. Although optimum BRB removal was obtained at pH 2.0, this pH is too acidic to be associated with real dye-polluted wastewaters. Therefore, we selected pH 4.0 for subsequent experiments due to its closer association with real dye polluted water and the higher uptake recorded compared to values from pH 5.0 to 9.0.

The influence of the initial concentration of dye on the removal of BRB onto ZnONP is shown in **Fig. 3b**. With the increase in BRB concentration from 10 to 50 mg/L, an increase in the adsorption capacity of ZnONP from 0.82 to 2.53 mg/g and a decrease in percentage adsorption from 82.1 to 50.6% was displayed. This trend is consistent with the findings of other researchers [26,61,62]. Thus as the BRB concentration in the aqueous phase increased, more BRB molecules were fixed on the active sites of ZnONPs, which resulted in site saturation, surface repulsions, and less percentage removal of dye from solution [63]. The BRB concentration of 50 mg/L was selected for the batch experiments due to the associated optimum adsorption capacity, which indicated effective utilization of the actives sites of the as-prepared ZnONP. On the other hand, the effect of ZnONP dosage on the removal of BRB on the adsorbent displayed an opposite trend to that of the initial dye concentration. As observed from **Fig. 3c**, with increasing dosage of ZnONP from 0.1 to 0.3 g, a decrease in the adsorption capacity from 2.53 to 1.17 mg/g and an increase in the percentage adsorption of BRB from 50.6 to 70.2% was recorded. Since the BRB concentration in solution was constant at 50 mg/L, as the dosage of ZnONP was increased, there was a corresponding increase in the active sites, thus accounting for the higher uptake of BRB from solution [56,64,65]. This in turn resulted in less saturation and less efficient use of the active sites of ZnONP due to decreasing BRB concentration in solution [5,66]. Hence, we utilized a ZnONP dosage of 0.1 g to enable optimum use of the active sites of the adsorbent.

Fig. 3d relates the influence of time on the removal of BRB onto ZnONP. A steady increase in both the percentage adsorption and adsorption capacity with an increase in time from 5 to 140 min was obtained. Thereafter, there was no noticeable change in the uptake of BRB onto ZnONP indicating that equilibrium was reached. At the initial stages of adsorption, the ZnONP sites were vacant and BRB concentration in solution was high [48]. This prompted a spontaneous interaction between the vacant sites and BRB molecules resulting in the initial rapid uptake. The interaction decreased with time due to the occupation of the sites of ZnONP as well as the reducing dye concentration in solution. Eventually equilibrium was achieved, attributed to the saturation of the sites on ZnONP [13]. A similar result was obtained in the abstraction of phenol from pharmaceutical and synthetic industrial wastewater onto ZnONP [67]. We maintained an adsorption time of 180 min to enable equilibrium in the uptake of BRB from the solution. Furthermore, the influence of solution temperature on the removal of BRB onto the synthesized ZnONP is illustrated in **Fig. 3e**. With an increase in solution temperature from 300 to 323 K, an increase in ZnONP adsorption capacity from 50.6 to 64.8%, and percentage adsorption of BRB from 2.53 to 3.24 mg/g were achieved. This suggests that the uptake of BRB on ZnONP is likely an endothermic one since it is favored at higher temperatures.

The improved BRB uptake at higher temperatures could be attributed to enhanced interaction between the BRB species in solution and the adsorption sites of ZnONP prompted by higher kinetic energy overcoming mass transfer resistances [68]. A similar finding was also documented in the uptake of As (III) from solution on ZnO nanorods [28].

Isotherm analysis of BRB adsorption

The adsorption isotherm modeling of BRB adsorption on the as-prepared ZnONP was conducted to obtain useful information on the favorability of the adsorption process, nature of adsorption as well as potent interaction between the two phases [56]. This was analyzed by the Langmuir, Temkin, Freundlich, and Flory-Huggins models as illustrated in **Fig. 4**. The calculated isotherm parameters obtained from the modeling are presented in **Table 2**. The best model fit was judged by the closer the R^2 value is to one and the smaller SSE. The Langmuir model, which depicts a monolayer dye uptake on a homogenous material surface [48], presented a lower R^2 and higher SSE than the Freundlich model and thus was not applicable in the description of BRB adsorption onto ZnONP. The Freundlich model gave the best fit to the process, presenting the highest R^2 of 0.9984 and lowest SSE of 0.0002. This implies a multilayer BRB uptake on a heterogeneous ZnONP surface and that physisorption must have played a major role in the overall removal process [5]. This result was not consistent with the report of other researchers on the adsorption of heavy metals, phenol and, dyes onto ZnONPs [26,28,29,67,69–71]. They deduced that the Langmuir model was more appropriate indicating a monolayer uptake of the pollutants on ZnONPs. However, our result corroborated the report by Khosla et al [72], that the Freundlich model presents a superior fit in the adsorption of anionic dyes (such as BRB) onto ZnONPs. Moreover, a good affinity between the adsorbent and pollutant in solution is usually indicated by the Freundlich n value within the range of 1 – 10 [29]. From Table 2, the n value was 2.304, which indicated efficient interaction between BRB species in solution and the ZnONP adsorbent. The favorability of the dye adsorption process was further tested by the application of the Langmuir separation factor [$R_L = (1/1 + K_L C_o)$][65]. Where K_L is the Langmuir equilibrium adsorption constant [70]. The R_L value denotes a linear ($R_L = 1$), an irreversible ($R_L = 0$), a favorable ($0< R_L<1$) and unfavorable ($R_L>1$) removal process [28]. The R_L value for BRB removal on ZnONP was in the range of 0.115 to 0.394, which corroborates the favorable adsorption of BRB, indicating that ZnONP is a viable adsorbent for the treatment of BRB polluted water. Besides, the monolayer uptake capacity of ZnONP for BRB was 3.099 mg/g, which is higher than that of activated charcoal (0.081 mg/g) [73] and polymeric gel (2.99 mg/g) [74] but lower than 22.72 mg/g obtained for chitin nanoparticle [75]. Thus, the simple preparation procedure as well as potent antifungal properties (see discussion in the “Antifungal activity” section) would be the advantage in the application of ZnONP for BRB wastewater treatment.

Table 2: The adsorption isotherm parameters for bromophenol blue adsorption onto ZnONP

Model	Parameter	Value
Langmuir	K_L (L/g)	0.154
	q_L (g/g)	3.099
	R^2	0.9852
	SSE	0.5219
Freundlich	N	2.304
	K_F (L/kg)	0.639
	R^2	0.9984
	SSE	0.0002
Temkin	B(g/g)	0.6495
	A (L/kg)	1.720
	R^2	0.9799
	SSE	0.0368
Flory-Huggins	n_{FH}	-2.048
	K_{FH}	0.0027
	R^2	0.9854
	SSE	0.0075

Kinetics and thermodynamics of adsorption

The kinetic modeling of adsorption processes helps in the calculation of kinetic parameters, which is useful in system design and provides useful information on sorption mechanism [76]. The kinetics of BRB adsorption onto ZnONP was modeled by the PFO, PSO, LFD, and IPD equations. The kinetic plots are presented in **Fig. 5** while the obtained kinetic parameters are given in **Table 3**. It is obvious from the R^2 of 0.9495 and the SSE of 0.7411 that the PSO was more suited than the PFO model in the kinetic description of BRB uptake onto ZnONP. This was also supported by the closer calculated qe (3.0597 mg/g) of the PSO to the experimental qe (2.53 mg/g), than that presented by the PFO model (3.4883 mg/g). The best fit presented by the PSO models suggests the involvement of electrostatic interactions between the BRB molecules in solution and ZnONP adsorbent in the dye removal process [77,78]. This implication corroborates our deduction from the FTIR analysis obtained after BRB adsorption onto ZnONP, which showed the involvement of electrostatic interactions. A similar result was reported in the adsorption of methylene blue onto ZnONP impregnated sawdust based cellulose nanocrystals [79].

Furthermore, the LFD and IPD models provide reliable information about the diffusion mechanism of adsorption [56]. Comparing the two diffusion models, it is evident that the IPD model was best fitted to the diffusion process of BRB molecules onto ZnONP as inferred from the high R^2 (0.9889) and low SSE (0.0581). This indicates that the diffusion of BRB through the surface pores of ZnONP played a vital role in the overall adsorption process than the boundary

layer diffusion. However, the occurrence of the intercept (0.1215), showed that particle diffusion was not solely responsible for BRB uptake, but to some extent involves film diffusion [29,48]. A similar finding in the adsorption of BRB onto *Solanum tuberosum* peel – silver nanoparticle hybrid was reported in our previous work [8]. The ultra-sonication applied prompted potent interaction between the dye species and the particle pores thus enhancing the particle diffusion mechanism. In addition, this observation is in line with the pore and SEM analysis, which showed a porous nature of ZnONP that, would enhance the dye uptake from the solution.

Table 3: The kinetic parameters for bromophenol blue adsorption onto ZnONP

Model	Parameter	Value
Pseudo-first order	$qe_{(exp)}$ (mg/g)	2.53
	K_l (min^{-1})	0.0264
	$qe_{(cal)}$ (mg/g)	3.4883
	R^2	0.8280
	SSE	0.7569
Pseudo-second-order	K_2 (g/mg min)	0.0073
	qe_{cal} (mg/g)	3.0597
	R^2	0.9495
	SSE	0.7411
Intraparticle diffusion	K_d (mg/g $min^{-1/2}$)	0.1858
	C	0.1215
	R^2	0.9889
	SSE	0.0581
Liquid film diffusion	K_{fd}	0.0264
	Y	0.3212
	R^2	0.8280
	SSE	4.0134

The thermodynamics of BRB adsorption on ZnONP was also evaluated from the Van't Hoff plot as illustrated in **Fig. 5e**. The calculated thermodynamic parameters such as the changes in enthalpy (ΔH^o), entropy (ΔS^o), and free energy (ΔG^o) were used to analyze the spontaneity, randomness, and the physical or chemical nature of BRB uptake onto the synthesized ZnONP [80]. The thermodynamic parameters obtained are presented in **Table 4**.

Table 4: Thermodynamic parameters for bromophenol blue adsorption onto ZnONP

Temp (K)	K_c	ΔG^o (kJ/mol)	ΔH^o (kJ/mol)	ΔS^o (J/mol K)	R^2
300	1.024	-0.059	22.173	74.02	0.9801
306	1.165	-0.387			
313	1.475	-1.012			
318	1.762	-1.498			
323	1.841	-1.638			

It is evident that the adsorption of BRB on the prepared ZnONP adsorbent is spontaneous as the ΔG^o values were negative at all temperatures [81]. Again, the increase in negativity of the ΔG^o values with temperature increase shows that high temperature is favorable for BRB uptake [82]. Also, the positive ΔH^o value recorded is a clear indication of the endothermic nature of the dye adsorption on ZnONP [83], which corroborates increasing BRB uptake with temperature increase (Fig. 3e). This result is consistent with other studies depicting the endothermic adsorption of As(III) [28], azo dyes [29] and, Pb(II) ions [71] on ZnONPs. It is important to mention that ΔH^o values in the range of 2.1 – 20.9 kJ/mol and 80 – 200 kJ/mol are attributed to physisorption and chemisorption respectively [84]. The ΔH^o of 22.173 kJ/mol obtained for the removal was slightly higher than the physisorption range but far lower than the chemisorption range. This indicated physicochemical adsorption of BRB onto ZnONP rather than a purely chemical or physical uptake, dominated mainly by the physical forces of adsorption [85]. Again, this implies that a much lower energy barrier is to be overcome in the desorption of the BRB loaded ZnONP during the regeneration of the adsorbent, compared to adsorption processes dominated or controlled by chemisorption. Furthermore, the increasing randomness at the ZnONP-BRB solution interface was indicated by the positive ΔS^o value of 74.02 J/molK [86]. This increasing random interaction at the interface must have enhanced efficient interaction between BRB molecules and the particle pores of ZnONP, which accounted for the dominant role played by intraparticle diffusion in the overall adsorption process. Such increasing randomness is well documented in the adsorption of dyes onto ZnONP based adsorbents [46,87–89].

Antifungal activity

The antifungal activity of the ZnONP is tested for possible application as simultaneous BRB removal and antifungal of wastewater. Noticeably, as shown in **Fig. 6**, all of the tested concentrations of ZnONP showed inhibitory effects on the three cultures, and the zones of inhibition increased consistently as the concentration of ZnONP increased **(Table 5).** The strain *A. alternata* CGJM 3076 showed maximum susceptibility towards ZnONP (0.002 – 5 mg/mL), as depicted by the largest zone of inhibition range from 25.09 – 36.28 mm. This was followed by *F. verticilliodes* CGJM 3823 (range from 23.77 – 34.77 mm) and *A. alternata* CGJM3078 (range from 22.73 – 30.63 mm). Concurrently, all the positive controls [bleach (5%)] exhibited similar diameter in their zones of inhibitions than those of ZnONP, while none of the negative control (sterile water) showed effects**.**

Significantly less volumes of ZnONP (40 µL) were used against all the tested fungi in this study in comparison to a previous study [32], where 100 µL volume was implemented for an identical concentrations range (0.002 – 5 mg/mL). The enhanced antifungal efficiency of the formulated ZnONP in the current study is possibly based on factors such as the size and shape of the particles, a large surface area to volume ratio that improved the solubility of the nanoparticles in comparison to the larger ones, the generation of reactive oxygen species (ROS) and the effective release of Zn^{2+} ions [50].

Table 5: Antifungal activities (*in vitro*) of ZnONP against the filamentous fungi *Alternaria alternata* (CGJM3078 andCGJM3006) and *Fusarium verticilliodes* CGJM 3823 are indicated in the form of inhibition zone sizes for each concentration of ZnONP treatment. The negative controls all did not show any activity.

ZnO NPs (mg/mL)	***Zone of Inhibition (mm)***					
	Alternaria alternata CGJM3078	Bleach (5%)	*Alternaria alternata* CGJM3006	Bleach (5%)	*Fusarium verticilliodes* CGJM 3823	Bleach (5%)
0.002	22.73	37.68	25.09	39.80	23.77	36.58
0.004	23.91	38.56	28.13	38.91	25.57	35.82
0.009	25.06	35.88	29.09	37.64	25.58	36.15
0.019	25.98	39.18	29.17	37.81	26.98	36.12
0.039	27.23	36.47	29.49	38.39	26.99	37.08
0.078	28.55	35.32	31.23	38.51	27.73	35.94
0.156	28.92	34.91	32.17	39.56	28.45	35.60
0.312	29.19	35.98	32.19	37.33	29.00	35.38
0.625	29.82	34.29	33.04	39.66	29.09	35.83
1.25	29.98	33.67	33.08	38.32	31.06	35.28
2.5	30.32	33.42	34.36	37.71	31.80	38.44
5	30.63	37.26	36.28	40.93	34.77	37.00

The exact underlying molecular mechanisms of ZnONP antifungal activities are yet to be elucidated [90]. In this study we proposed a few plausible mechanisms **(Fig. 7).** Zn^{2+} can possibly be released from the surface of ZnONP, as it has been shown in AgNPs [91] that interacted with the fungal cell wall, passed and accumulated in the cytoplasm. This causes cell metabolism disturbances, impairment of the nucleic acid material by their irreversible adherence, ribosome disassembly, protein denaturations, electron chain disruptions, all of which ultimately resulting in cell death (Fig. 7). The interactions may also cause deformed fungal hyphae with ruptures and unusual bulging as was observed in an SEM study of antifungal activities of Zn compounds against pathogenic fungal strains of *Fusarium graminearum, Penicillium citrinum and Aspergillus flavus* [92]. The generation of the reactive oxygen species (ROS) (Fig. 7) as per a previous study [50], can cause lipid peroxidation, leading to cell death. Simultaneously, the fungal cell wall can become more permeable because of the Zn^{2+}, resulting in subsequent leakage of the plasma fluid and cellular organelles causing cellular senescence **(Fig. 7)**. SEM structure imaging of the ZnONP developed in the present study revealed the average size of ZnONP as 65.3 nm. This is consistent with the previous findings [30], where the average size was reported as 70 ± 15 nm. Those ZnONPs successfully inhibited the growth of mycotoxin producing fungi, *Botrytis cinerea* and *Penicillium expansum*, causing cellular perturbations, and fungal hyphal distortion.

Conclusions

Zinc oxide nanoparticle (ZnONP) was synthesized in a- simple one-pot system and applied for the adsorption of bromophenol blue (BRB) and as an antifungal agent against *Alternaria alternata* and *Fusarium verticilliodes* filamentous fungi. The FTIR showed the presence of the O-H and Zn-O bands on the synthesized ZnONP, which were responsible for the adsorption of BRB via electrostatic, hydrophobic, and weak Vander Waals interaction. The XRD, UV, and EDX characterizations showed the successful synthesis of the ZnONP. Thermal analysis revealed high thermal stability of the ZnONP with a 22.92% weight loss at 800 ^{o}C, while BET analysis showed sufficient surface area and pore properties desirable for efficient BRB uptake from solution. The SEM and TEM morphology displayed an irregular shaped and aggregated porous structure of ZnONPs. The solution temperature, pH, time, BRB concentration, and ZnONP dosage were found to influence significantly the BRB uptake on ZnONP. The operating conditions were selected as pH, temperature, time, dosage, and concentration of 4.0, 300 K, 180 min, 0.1 g, and 50 mg/L respectively. The Freundlich model presented the best fit to the isotherm analysis for the adsorption process compared to the Langmuir, Flory Huggins, and Temkin isotherm models. For kinetic analysis of BRB adsorption onto ZnONP, the pseudo-second-order and intra-particle-diffusion were better fitted than the Pseudo-first-order and liquid-film-diffusion models. A feasible, spontaneous, random, and endothermic removal of BRB onto ZnONP was revealed from the thermodynamic evaluation of the process. The synthesized ZnONP was found to be efficient in the adsorption of BRB from solution with a maximum monolayer uptake capacity of 3.099 mg/g, which was higher than some previously reported adsorbents.

In addition, the prepared ZnONP exhibited potent antifungal activities against the filamentous fungi, *A. alternata* and *F. verticilliodes*. The antifungal effects, such as inhibition of growth and reproduction of the filamentous fungi, are enhanced significantly with the ZnO nanostructures. Therefore, the present study, together with previous studies, showed that ZnONP have tremendous potential as an effective postharvest disease control antifungal agents against filamentous fungi, or even possibly in the field. No studies have, however, tested this in vivo.

Declarations

Acknowledgment

KGA and SG appreciate the postdoctoral support of the University of the Free State, South Africa. We also thank the management of the physical chemistry and Genetics laboratories of the University of the Free State, for the conducive environment to conduct this research.

Author Contributions

KGA and SG, conceptualized the research, conducted laboratory experiments, analyzed the obtained data and wrote the manuscript. MG and JC supervised, read and edited the manuscript and provided financial support to conduct the research.

References

1. Tohamy, H.-A. S., El-Sakhawy, M. & Kamel, S. Carboxymethyl Cellulose-Grafted Graphene Oxide/Polyethylene Glycol for Efficient Ni(II) Adsorption. *J. Polym. Environ.* (2020) doi:10.1007/s10924-020-01920-7.
2. Al-Ghouti, M. A. & Al-Absi, R. S. Mechanistic understanding of the adsorption and thermodynamic aspects of cationic methylene blue dye onto cellulosic olive stones biomass from wastewater. *Sci. Rep.***10**, 15928 (2020).

3. Tian, B., Hua, S., Tian, Y. & Liu, J. Cyclodextrin-based adsorbents for the removal of pollutants from wastewater: a review. *Environ. Sci. Pollut. Res.* (2020) doi:10.1007/s11356-020-11168-2.
4. Dotto, G. L. & McKay, G. Current scenario and challenges in adsorption for water treatment. *J. Environ. Chem. Eng.***8**, 103988 (2020).
5. Akpomie, K. G. & Conradie, J. Banana peel as a biosorbent for the decontamination of water pollutants. A review. *Environ. Chem. Lett.***18**, 1085–1112 (2020).
6. Yagub, M. T., Sen, T. K., Afroze, S. & Ang, H. M. Dye and its removal from aqueous solution by adsorption: A review. *Adv. Colloid Interface Sci.***209**, 172–184 (2014).
7. Mirzaei, D., Zabardasti, A., Mansourpanah, Y., Sadeghi, M. & Farhadi, S. Efficacy of Novel NaX/MgO–TiO2 Zeolite Nanocomposite for the Adsorption of Methyl Orange (MO) Dye: Isotherm, Kinetic and Thermodynamic Studies. *J. Inorg. Organomet. Polym. Mater.***30**, 2067–2080 (2020).
8. Akpomie, K. G. & Conradie, J. Biogenic and chemically synthesized Solanum tuberosum peel–silver nanoparticle hybrid for the ultrasonic aided adsorption of bromophenol blue dye. *Sci. Rep.***10**, 17094 (2020).
9. Wang, J. *et al.* Preparation and excellent adsorption of water pollution dyes over magnetic Fe3O4/C nanoparticles with hollow grape cluster morphology. *J. Nanoparticle Res.***22**, 196 (2020).
10. Mok, C. F. *et al.* Adsorption of Dyes Using Poly(vinyl alcohol) (PVA) and PVA-Based Polymer Composite Adsorbents: A Review. *J. Polym. Environ.***28**, 775–793 (2020).
11. El-Gamal, S. M. A., Amin, M. S. & Ahmed, M. A. Removal of methyl orange and bromophenol blue dyes from aqueous solution using Sorel's cement nanoparticles. *J. Environ. Chem. Eng.***3**, 1702–1712 (2015).
12. Akpomie, K. G. & Conradie, J. Efficient synthesis of magnetic nanoparticle-Musa acuminata peel composite for the adsorption of anionic dye. *Arab. J. Chem.***13**, 7115–7131 (2020).
13. Saghian, M., Dehghanpour, S. & Sharbatdaran, M. Unique and efficient adsorbents for highly selective and reverse adsorption and separation of dyes via the introduction of SO 3 H functional groups into a metal–organic framework. *RSC Adv.***10**, 9369–9377 (2020).
14. Song, Y.-B., Song, X.-D., Cheng, C.-J. & Zhao, Z.-G. Poly(4-styrenesulfonic acid-co-maleic acid)-sodium-modified magnetic reduced graphene oxide for enhanced adsorption performance toward cationic dyes. *RSC Adv.***5**, 87030–87042 (2015).
15. Ani, J. U. *et al.* Potentials of activated carbon produced from biomass materials for sequestration of dyes, heavy metals, and crude oil components from aqueous environment. *Appl. Water Sci.***10**, 1–11 (2020).
16. Song, F. *et al.* Adsorption kinetics and thermodynamics of Ni (II) by Pisha sandstone. *J. Nanoparticle Res.***22**, 179 (2020).
17. Anastopoulos, I., Hosseini-Bandegharaei, A., Fu, J., Mitropoulos, A. C. & Kyzas, G. Z. Use of nanoparticles for dye adsorption: Review. *J. Dispers. Sci. Technol.***39**, 836–847 (2018).
18. Kausar, A. *et al.* Dyes adsorption using clay and modified clay: A review. *J. Mol. Liq.***256**, 395–407 (2018).
19. Reyes-Ledezma, J. L., Uribe-Ramírez, D., Cristiani-Urbina, E. & Morales-Barrera, L. Biosorptive removal of acid orange 74 dye by HCl-pretreated Lemna sp. *PLoS One***15**, e0228595 (2020).
20. Wong, S. *et al.* Effective removal of anionic textile dyes using adsorbent synthesized from coffee waste. *Sci. Rep.***10**, 2928 (2020).
21. David, M. K., Okoro, U. C., Akpomie, K. G., Okey, C. & Oluwasola, H. O. Thermal and hydrothermal alkaline modification of kaolin for the adsorptive removal of lead(II) ions from aqueous solution. *SN Appl. Sci.***2**, 1134 (2020).

22. Cui, Z., Zhang, J., Xue, Y. & Duan, H. Size-Dependent Thermodynamics and Kinetics of Adsorption on Nanoparticles: A Theoretical and Experimental Study. *Langmuir***34**, 3197–3206 (2018).
23. Marimuthu, S. *et al.* Silver nanoparticles in dye effluent treatment: A review on synthesis, treatment methods, mechanisms, photocatalytic degradation, toxic effects and mitigation of toxicity. *J. Photochem. Photobiol. B Biol.***205**, 111823 (2020).
24. Al-Aoh, H. A. Adsorption performances of nickel oxide nanoparticles (NiO NPs) towards bromophenol blue dye (BB). *Desalin. WATER Treat.***110**, 229–238 (2018).
25. Ahmed, M. A. & Abou-Gamra, Z. M. Mesoporous MgO nanoparticles as a potential sorbent for removal of fast orange and bromophenol blue dyes. *Nanotechnol. Environ. Eng.***1**, 10 (2016).
26. Gu, M. *et al.* The selective heavy metal ions adsorption of zinc oxide nanoparticles from dental wastewater. *Chem. Phys.***534**, 110750 (2020).
27. Akbar, A. *et al.* Synthesis and antimicrobial activity of zinc oxide nanoparticles against foodborne pathogens Salmonella typhimurium and Staphylococcus aureus. *Biocatal. Agric. Biotechnol.***17**, 36–42 (2019).
28. Yuvaraja, G., Prasad, C., Vijaya, Y. & Subbaiah, M. V. Application of ZnO nanorods as an adsorbent material for the removal of As(III) from aqueous solution: kinetics, isotherms and thermodynamic studies. *Int. J. Ind. Chem.***9**, 17–25 (2018).
29. Zafar, M. N. *et al.* Effective adsorptive removal of azo dyes over spherical ZnO nanoparticles. *J. Mater. Res. Technol.***8**, 713–725 (2019).
30. He, L., Liu, Y., Mustapha, A. & Lin, M. Antifungal activity of zinc oxide nanoparticles against Botrytis cinerea and Penicillium expansum. *Microbiol. Res.***166**, 207–215 (2011).
31. Arciniegas-Grijalba, P. A., Patiño-Portela, M. C., Mosquera-Sánchez, L. P., Guerrero-Vargas, J. A. & Rodríguez-Páez, J. E. ZnO nanoparticles (ZnO-NPs) and their antifungal activity against coffee fungus Erythricium salmonicolor. *Appl. Nanosci.***7**, 225–241 (2017).
32. De la Rosa-García, S. C. *et al.* Antifungal Activity of ZnO and MgO Nanomaterials and Their Mixtures against Colletotrichum gloeosporioides Strains from Tropical Fruit. *J. Nanomater.***2018**, 1–9 (2018).
33. Souza, R. C. de, Haberbeck, L. U., Riella, H. G., Ribeiro, D. H. B. & Carciofi, B. A. M. Antibacterial activity of zinc oxide nanoparticles synthesized by solochemical process. *Brazilian J. Chem. Eng.***36**, 885–893 (2019).
34. Gambino, M., Ahmed, M. A. A., Villa, F. & Cappitelli, F. Zinc oxide nanoparticles hinder fungal biofilm development in an ancient Egyptian tomb. *Int. Biodeterior. Biodegradation***122**, 92–99 (2017).
35. Sardella, D., Gatt, R. & Valdramidis, V. P. Physiological effects and mode of action of ZnO nanoparticles against postharvest fungal contaminants. *Food Res. Int.***101**, 274–279 (2017).
36. Reddy, M. V. B., Angers, P., Castaigne, F. & Arul, J. Chitosan Effects on Blackmold Rot and Pathogenic Factors Produced by Alternaria alternata in Postharvest Tomatoes. *J. Am. Soc. Hortic. Sci.***125**, 742–747 (2000).
37. Tsuge, T. *et al.* Host-selective toxins produced by the plant pathogenic fungus Alternaria alternata. *FEMS Microbiol. Rev.***37**, 44–66 (2013).
38. Pastor, F. J. & Guarro, J. Alternaria infections: laboratory diagnosis and relevant clinical features. *Clin. Microbiol. Infect.***14**, 734–746 (2008).
39. Baldwin, T. T. *et al.* Maize Seedling Blight Induced by Fusarium verticillioides : Accumulation of Fumonisin B 1 in Leaves without Colonization of the Leaves. *J. Agric. Food Chem.***62**, 2118–2125 (2014).
40. Janse van Rensburg, B., Mc Laren, N. W., Schoeman, A. & Flett, B. C. The effects of cultivar and prophylactic fungicide spray for leaf diseases on colonisation of maize ears by fumonisin producing Fusarium spp. and

fumonisin synthesis in South Africa. *Crop Prot.***79**, 56–63 (2016).

41. Zhang, L., Wang, J., Zhang, C. & Wang, Q. Analysis of potential fumonisin-producing Fusarium species in corn products from three main maize-producing areas in eastern China. *J. Sci. Food Agric.***93**, 693–701 (2013).
42. Gallo, A., Giuberti, G., Frisvad, J., Bertuzzi, T. & Nielsen, K. Review on Mycotoxin Issues in Ruminants: Occurrence in Forages, Effects of Mycotoxin Ingestion on Health Status and Animal Performance and Practical Strategies to Counteract Their Negative Effects. *Toxins (Basel).***7**, 3057–3111 (2015).
43. Chandra Nayaka, S. *et al.* Control of Fusarium verticillioides , cause of ear rot of maize, by Pseudomonas fluorescens. *Pest Manag. Sci.***65**, 769–775 (2009).
44. Marin, S., Ramos, A. J., Cano-Sancho, G. & Sanchis, V. Mycotoxins: Occurrence, toxicology, and exposure assessment. *Food Chem. Toxicol.***60**, 218–237 (2013).
45. Wu, F. Measuring the economic impacts of Fusarium toxins in animal feeds. *Anim. Feed Sci. Technol.***137**, 363–374 (2007).
46. Akpomie, K. G. & Conradie, J. Synthesis, characterization, and regeneration of an inorganic–organic nanocomposite (ZnO@biomass) and its application in the capture of cationic dye. *Sci. Rep.***10**, 14441 (2020).
47. Jiao, Y. *et al.* Characterization of pine-sawdust pyrolytic char activated by phosphoric acid through microwave irradiation and adsorption property toward CDNB in batch mode. *Desalin. Water Treat.***77**, 247–255 (2017).
48. Ezekoye, O. M. *et al.* Biosorptive interaction of alkaline modified Dialium guineense seed powders with ciprofloxacin in contaminated solution: central composite, kinetics, isotherm, thermodynamics, and desorption. *Int. J. Phytoremediation***22**, 1028–1037 (2020).
49. Ghosh, S. *et al.* In Situ Cultured Bacterial Diversity from Iron Curtain Cave, Chilliwack, British Columbia, Canada. *Diversity***9**, 36 (2017).
50. Kumar, P. *et al.* Optical and surface properties of Zn doped CdO nanorods and antimicrobial applications. *Colloids Surfaces A Physicochem. Eng. Asp.***605**, 125369 (2020).
51. Selim, Y. A., Azb, M. A., Ragab, I. & H. M. Abd El-Azim, M. Green Synthesis of Zinc Oxide Nanoparticles Using Aqueous Extract of Deverra tortuosa and their Cytotoxic Activities. *Sci. Rep.***10**, 3445 (2020).
52. Jayappa, M. D. *et al.* Green synthesis of zinc oxide nanoparticles from the leaf, stem and in vitro grown callus of Mussaenda frondosa L.: characterization and their applications. *Appl. Nanosci.***10**, 3057–3074 (2020).
53. Sharifalhoseini, Z., Entezari, M. H. & Jalal, R. Direct and indirect sonication affect differently the microstructure and the morphology of ZnO nanoparticles: Optical behavior and its antibacterial activity. *Ultrason. Sonochem.***27**, 466–473 (2015).
54. Ramimoghadam, D., Hussein, M. Z. Bin & Taufiq-Yap, Y. H. Synthesis and characterization of ZnO nanostructures using palm olein as biotemplate. *Chem. Cent. J.***7**, 71 (2013).
55. Ali, I., Peng, C. & Naz, I. Removal of lead and cadmium ions by single and binary systems using phytogenic magnetic nanoparticles functionalized by 3-marcaptopropanic acid. *Chinese J. Chem. Eng.***27**, 949–964 (2019).
56. Chukwuemeka-Okorie, H. O., Ekemezie, P. N., Akpomie, K. G. & Olikagu, C. S. Calcined corncob-kaolinite Combo as new sorbent for sequestration of toxic metal ions from polluted aqua media and desorption. *Front. Chem.***6**, 1–13 (2018).
57. Haque, M. J., Bellah, M. M., Hassan, M. R. & Rahman, S. Synthesis of ZnO nanoparticles by two different methods & comparison of their structural, antibacterial, photocatalytic and optical properties. *Nano Express***1**, 010007 (2020).

58. Mahamuni, P. P. *et al.* Synthesis and characterization of zinc oxide nanoparticles by using polyol chemistry for their antimicrobial and antibiofilm activity. *Biochem. Biophys. Reports***17**, 71–80 (2019).
59. Afroze, S. & Sen, T. K. A Review on Heavy Metal Ions and Dye Adsorption from Water by Agricultural Solid Waste Adsorbents. *Water. Air. Soil Pollut.***229**, (2018).
60. Joudi, M. *et al.* Synthesis of an efficient hydroxyapatite–chitosan–montmorillonite thin film for the adsorption of anionic and cationic dyes: adsorption isotherm, kinetic and thermodynamic study. *SN Appl. Sci.***2**, 1078 (2020).
61. Silva, F. *et al.* Biosorption of Methylene Blue Dye Using Natural Biosorbents Made from Weeds. *Materials (Basel).***12**, 2486 (2019).
62. Cai, C.-X. *et al.* A novel approach of utilization of the fungal conidia biomass to remove heavy metals from the aqueous solution through immobilization. *Sci. Rep.***6**, 36546 (2016).
63. Lin, D. *et al.* Adsorption of Dye by Waste Black Tea Powder: Parameters, Kinetic, Equilibrium, and Thermodynamic Studies. *J. Chem.***2020**, 1–13 (2020).
64. Rokni, S., Haji Seyed Mohammad Shirazi, R., Miralinaghi, M. & Moniri, E. Efficient adsorption of anionic dyes onto magnetic graphene oxide coated with polyethylenimine: Kinetic, isotherm, and thermodynamic studies. *Res. Chem. Intermed.***46**, 2247–2274 (2020).
65. Raghav, S. & Kumar, D. Adsorption Equilibrium, Kinetics, and Thermodynamic Studies of Fluoride Adsorbed by Tetrametallic Oxide Adsorbent. *J. Chem. Eng. Data***63**, 1682–1697 (2018).
66. Hamzezadeh, A., Rashtbari, Y., Afshin, S., Morovati, M. & Vosoughi, M. Application of low-cost material for adsorption of dye from aqueous solution. *Int. J. Environ. Anal. Chem.* 1–16 (2020) doi:10.1080/03067319.2020.1720011.
67. Sridar, R., Ramanane, U. U. & Rajasimman, M. ZnO nanoparticles – Synthesis, characterization and its application for phenol removal from synthetic and pharmaceutical industry wastewater. *Environ. Nanotechnology, Monit. Manag.***10**, 388–393 (2018).
68. Mustapha, S. *et al.* Adsorption isotherm, kinetic and thermodynamic studies for the removal of Pb(II), Cd(II), Zn(II) and Cu(II) ions from aqueous solutions using Albizia lebbeck pods. *Appl. Water Sci.***9**, 142 (2019).
69. Sheela, T., Nayaka, Y. A., Viswanatha, R., Basavanna, S. & Venkatesha, T. G. Kinetics and thermodynamics studies on the adsorption of Zn(II), Cd(II) and Hg(II) from aqueous solution using zinc oxide nanoparticles. *Powder Technol.***217**, 163–170 (2012).
70. Zhang, F., Chen, X., Wu, F. & Ji, Y. High adsorption capability and selectivity of ZnO nanoparticles for dye removal. *Colloids Surfaces A Physicochem. Eng. Asp.***509**, 474–483 (2016).
71. Azizi, S., Mahdavi Shahri, M. & Mohamad, R. Green Synthesis of Zinc Oxide Nanoparticles for Enhanced Adsorption of Lead Ions from Aqueous Solutions: Equilibrium, Kinetic and Thermodynamic Studies. *Molecules***22**, 831 (2017).
72. Khosla, E., Kaur, S. & Dave, P. N. Ionic dye adsorption by zinc oxide nanoparticles. *Chem. Ecol.***31**, 173–185 (2015).
73. Iqbal, M. J. & Ashiq, M. N. Adsorption of dyes from aqueous solutions on activated charcoal. *J. Hazard. Mater.***139**, 57–66 (2007).
74. Malana, M. A., Ijaz, S. & Ashiq, M. N. Removal of various dyes from aqueous media onto polymeric gels by adsorption process: Their kinetics and thermodynamics. *Desalination***263**, 249–257 (2010).
75. Dhananasekaran, S., Palanivel, R. & Pappu, S. Adsorption of Methylene Blue, Bromophenol Blue, and Coomassie Brilliant Blue by α-chitin nanoparticles. *J. Adv. Res.***7**, 113–124 (2016).

76. Tambat, S. N., Ahirrao, D. J., Pandit, A. B., Jha, N. & Sontakke, S. M. Hydrothermally synthesized N2-UiO-66 for enhanced and selective adsorption of cationic dyes. *Environ. Technol. Innov.***19**, 101021 (2020).
77. Mishra, S. R., Chandra, R., Kaila A., J. & Darshi B., S. Kinetics and isotherm studies for the adsorption of metal ions onto two soil types. *Environ. Technol. Innov.***7**, 87–101 (2017).
78. Vishan, I., Saha, B., Sivaprakasam, S. & Kalamdhad, A. Evaluation of Cd(II) biosorption in aqueous solution by using lyophilized biomass of novel bacterial strain Bacillus badius AK: Biosorption kinetics, thermodynamics and mechanism. *Environ. Technol. Innov.***14**, 100323 (2019).
79. Oyewo, O. A., Adeniyi, A., Sithole, B. B. & Onyango, M. S. Sawdust-Based Cellulose Nanocrystals Incorporated with ZnO Nanoparticles as Efficient Adsorption Media in the Removal of Methylene Blue Dye. *ACS Omega***5**, 18798–18807 (2020).
80. Ma, Y. *et al.* Iron/zinc and phosphoric acid modified sludge biochar as an efficient adsorbent for fluoroquinolones antibiotics removal. *Ecotoxicol. Environ. Saf.***196**, 110550 (2020).
81. Yan, Y. *et al.* Phosphorus-rich biochar produced through bean-worm skin waste pyrolysis enhances the adsorption of aqueous lead. *Environ. Pollut.***266**, 115177 (2020).
82. Al-Senani, G. M. & Al-Fawzan, F. F. Adsorption study of heavy metal ions from aqueous solution by nanoparticle of wild herbs. *Egypt. J. Aquat. Res.***44**, 187–194 (2018).
83. Dong, Y. *et al.* Influence of microwave-assisted synthesis on the structural and textural properties of mesoporous MIL-101(Fe) and NH2-MIL-101(Fe) for enhanced tetracycline adsorption. *Mater. Chem. Phys.***251**, 123060 (2020).
84. Saffarionpour, S., Tam, S.-Y. S., Van der Wielen, L. A. M., Brouwer, E. & Ottens, M. Influence of ethanol and temperature on adsorption of flavor-active esters on hydrophobic resins. *Sep. Purif. Technol.***210**, 219–230 (2019).
85. Liang, S., Guo, X., Feng, N. & Tian, Q. Isotherms, kinetics and thermodynamic studies of adsorption of Cu2+ from aqueous solutions by Mg2+/K+ type orange peel adsorbents. *J. Hazard. Mater.***174**, 756–762 (2010).
86. Ahmad, A. A., Din, A. T. M., Yahaya, N. K. E., Khasri, A. & Ahmad, M. A. Adsorption of basic green 4 onto gasified Glyricidia sepium woodchip based activated carbon: Optimization, characterization, batch and column study. *Arab. J. Chem.***13**, 6887–6903 (2020).
87. Priyadarshini, B., Behera, S. S., Rath, P. P., Sahoo, T. R. & Parhi, P. K. Adsorption of xylenol orange dye on nano ZnO: Kinetics, thermodynamics and isotherm study. in *AIP confrences series* 050043 (2017). doi:10.1063/1.4980276.
88. Elfeky, A. S., Youssef, H. F. & Elzaref, A. S. Adsorption of Dye from Wastewater onto ZnO Nanoparticles-Loaded Zeolite: Kinetic, Thermodynamic and Isotherm Studies. *Zeitschrift für Phys. Chemie***234**, 255–278 (2020).
89. Zhang, M., Chang, L., Zhao, Y. & Yu, Z. Fabrication of Zinc Oxide/Polypyrrole Nanocomposites for Brilliant Green Removal from Aqueous Phase. *Arab. J. Sci. Eng.***44**, 111–121 (2019).
90. Moritz, M. & Geszke-Moritz, M. The newest achievements in synthesis, immobilization and practical applications of antibacterial nanoparticles. *Chem. Eng. J.***228**, 596–613 (2013).
91. Rai, M., Yadav, A. & Gade, A. Silver nanoparticles as a new generation of antimicrobials. *Biotechnol. Adv.***27**, 76–83 (2009).
92. Savi, G. D., Bortoluzzi, A. J. & Scussel, V. M. Antifungal properties of Zinc-compounds against toxigenic fungi and mycotoxin. *Int. J. Food Sci. Technol.***48**, 1834–1840 (2013).

Figures

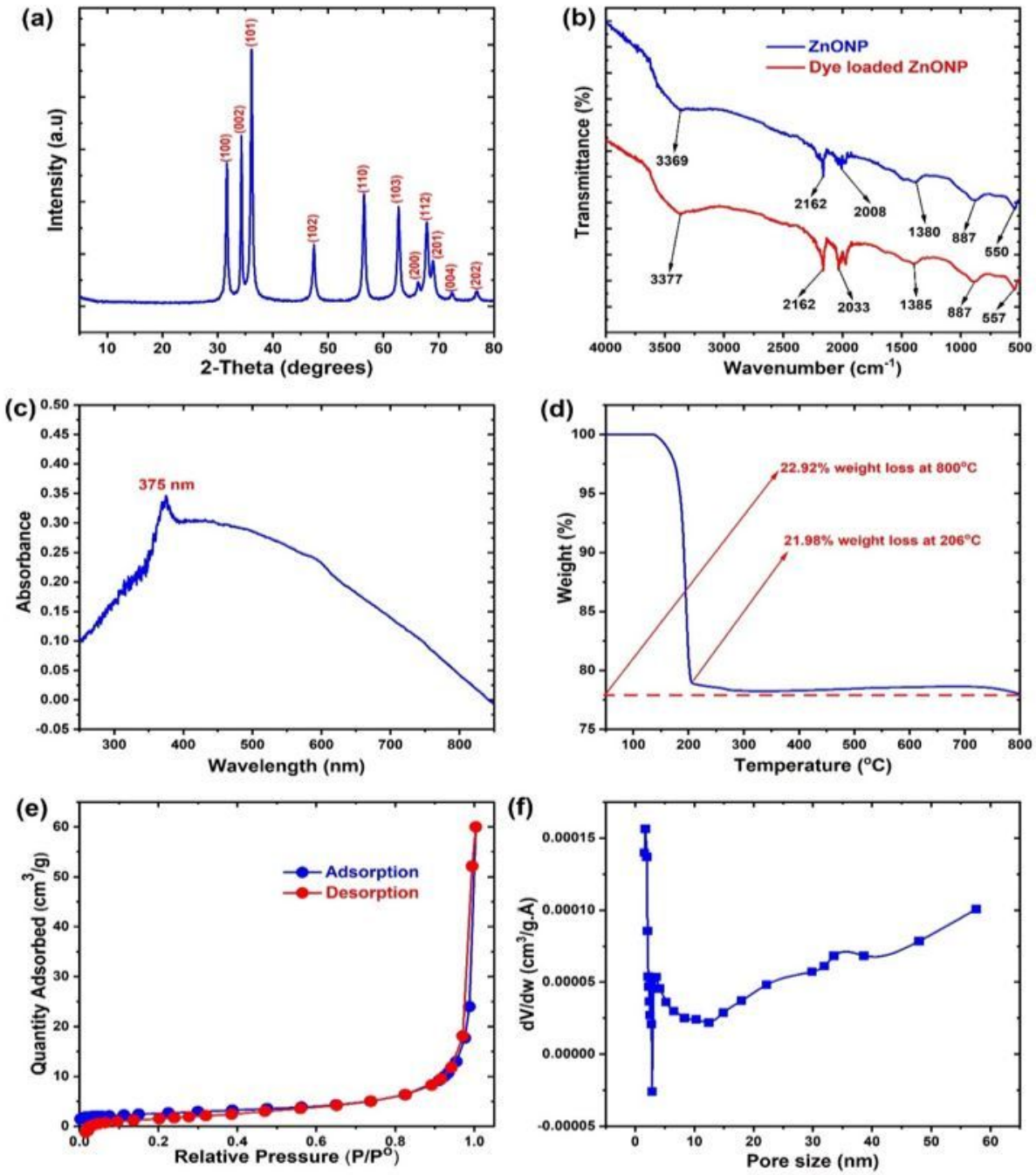

Figure 1

The (a) X-ray diffraction (b) Fourier transform infrared (c) Ultraviolent spectra (d) Thermogravimetric analysis (e) Nitrogen adsorption-desorption isotherm and (f) Pore analysis of the synthesized ZnONP.

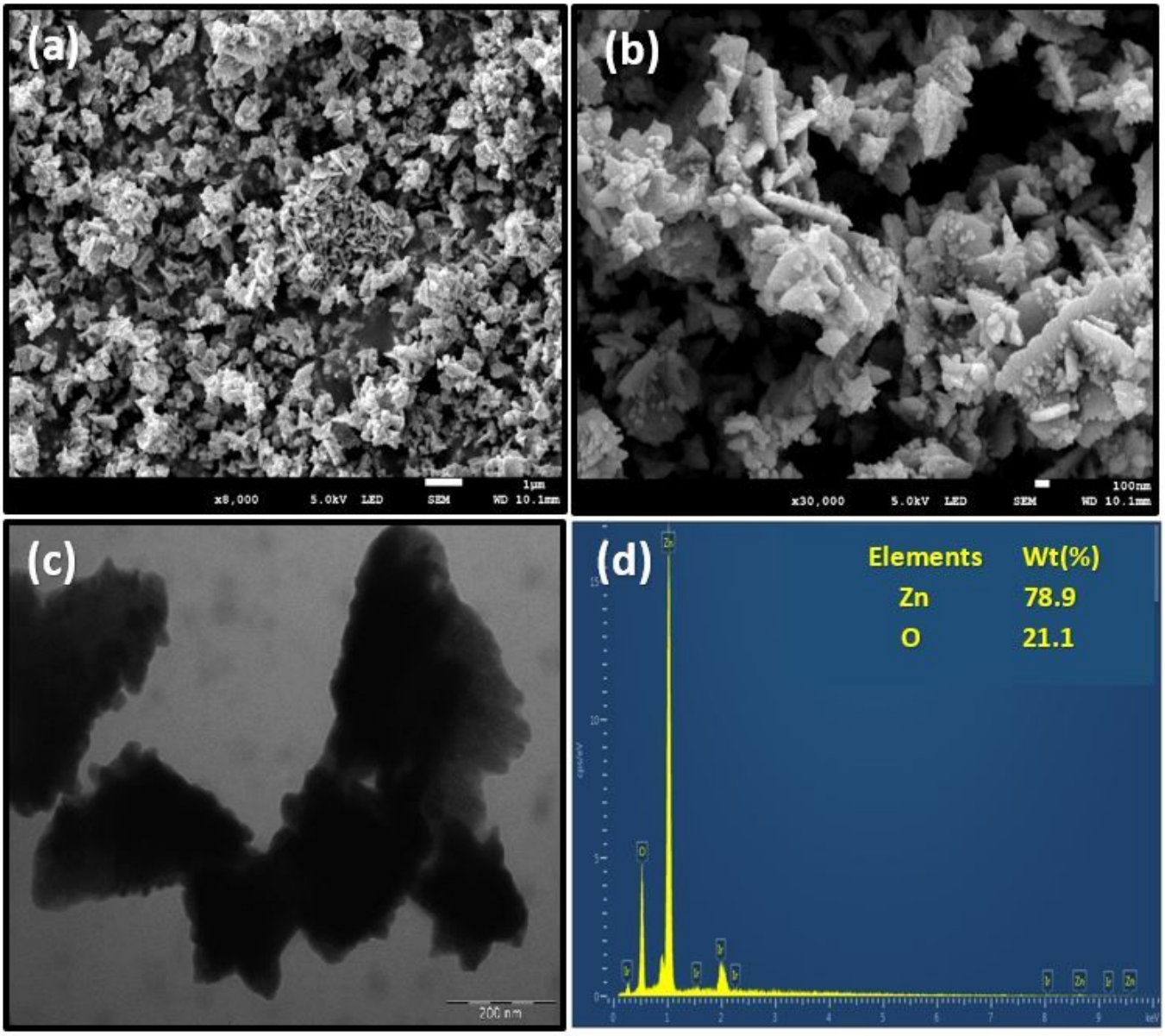

Figure 2

The (a, b) Scanning Electron microscopy (c) Transmission electron microscopy and (d) Energy dispersive X-ray spectrum of the synthesized ZnONP.

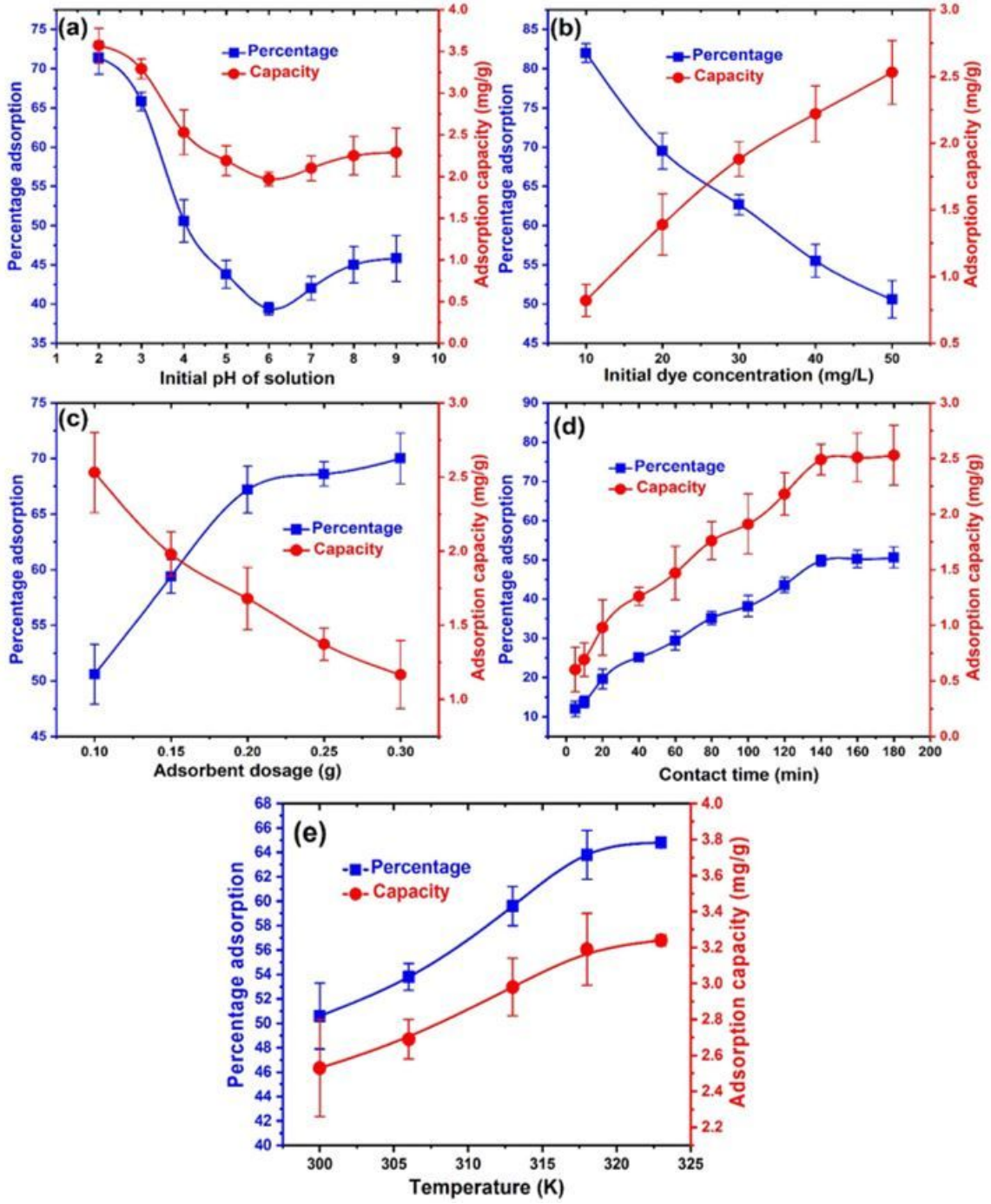

Figure 3

The influence of (a) solution pH (b) BRB concentration (c) ZnONP dosage (d) contact time and (e) solution temperature on the removal of BRB onto ZnONP.

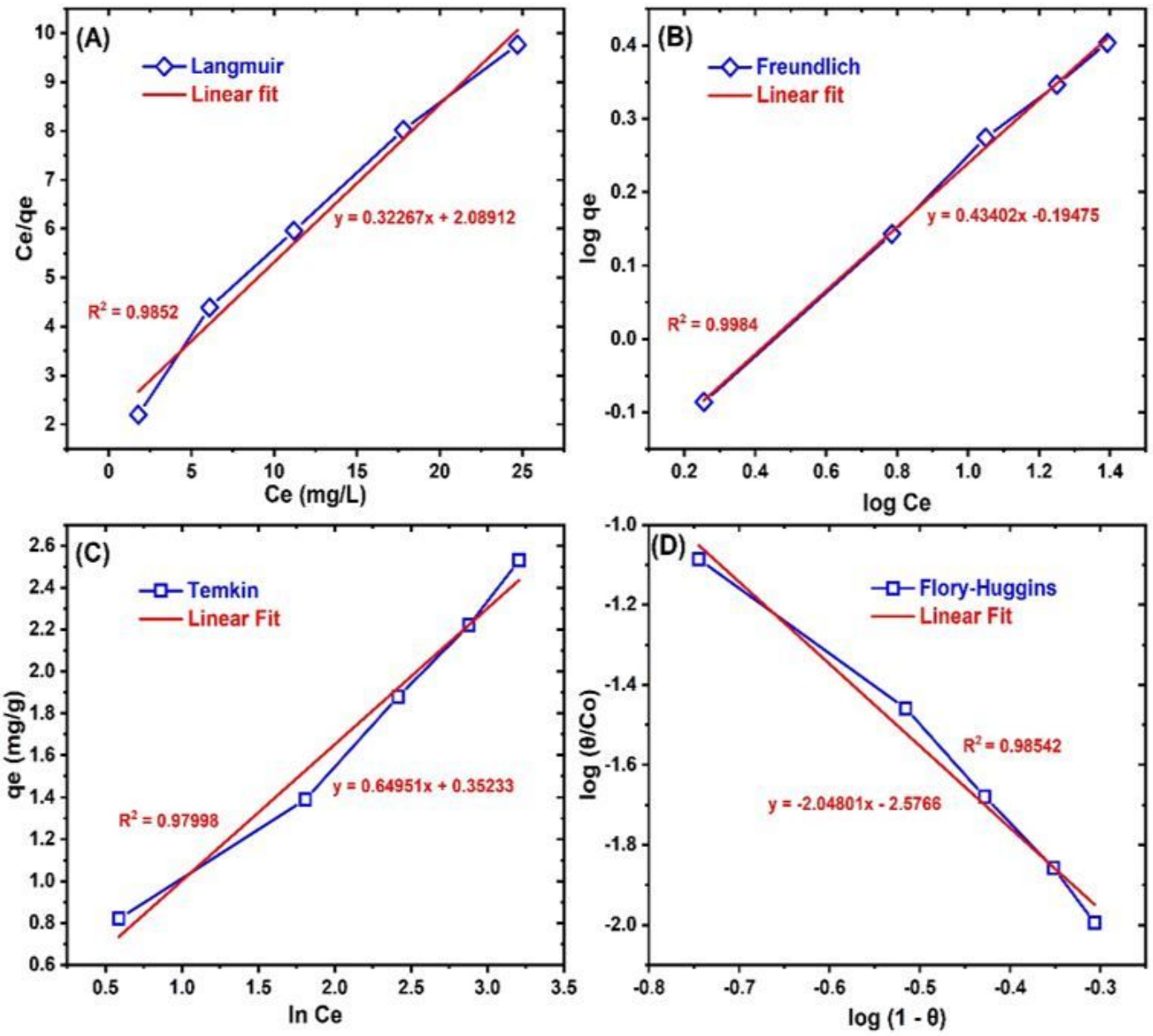

Figure 4

The (a) Langmuir (b) Freundlich (c) Temkin and (d) Flory-Huggins isotherm plots for the adsorption of BRP onto ZnONP.

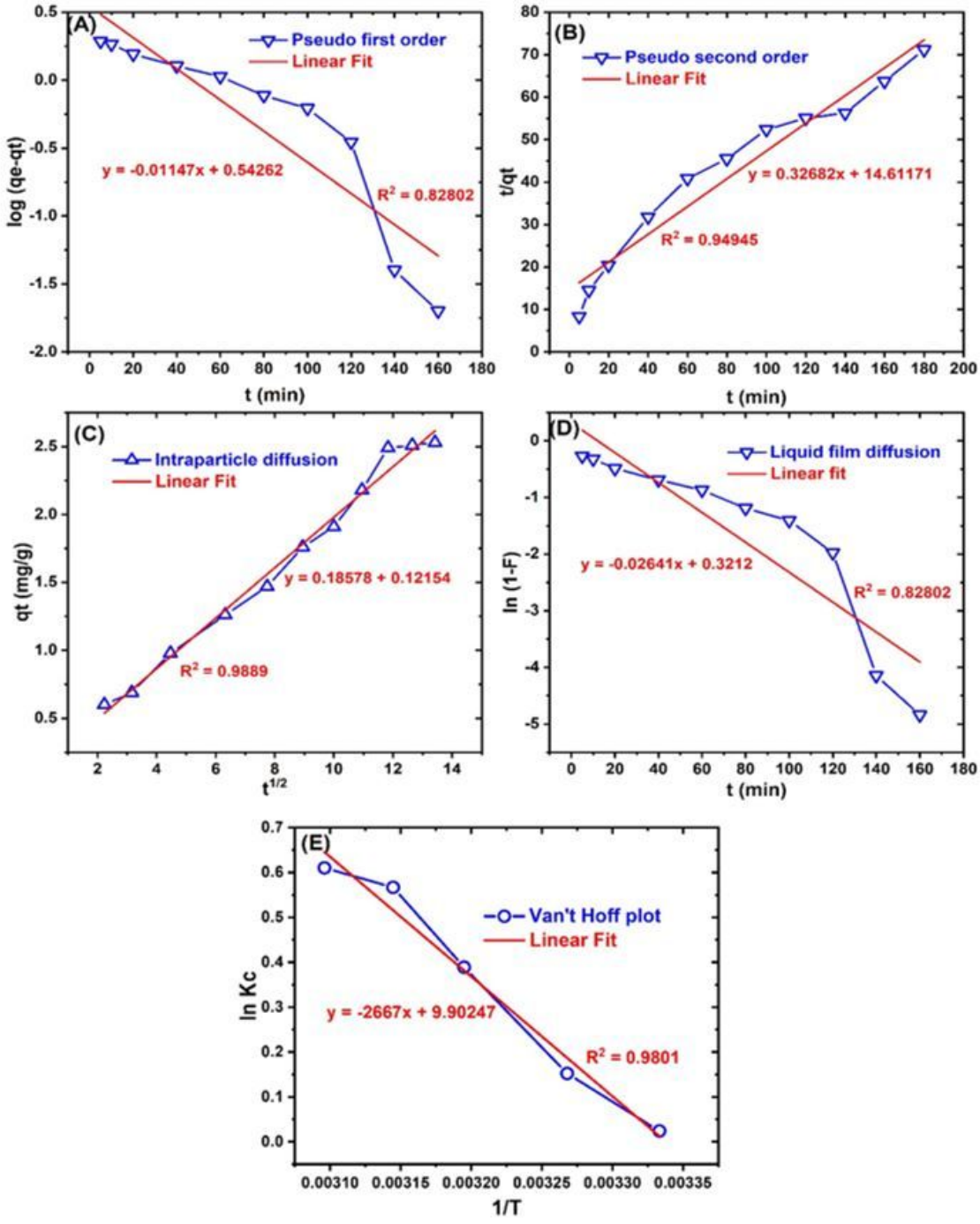

Figure 5

The (a) Pseudo-first-order (b) Pseudo-second order (c) Intraparticle diffusion (d) liquid film diffusion and (e) Van't Hoff plots for the adsorption of BRP onto ZnONP.

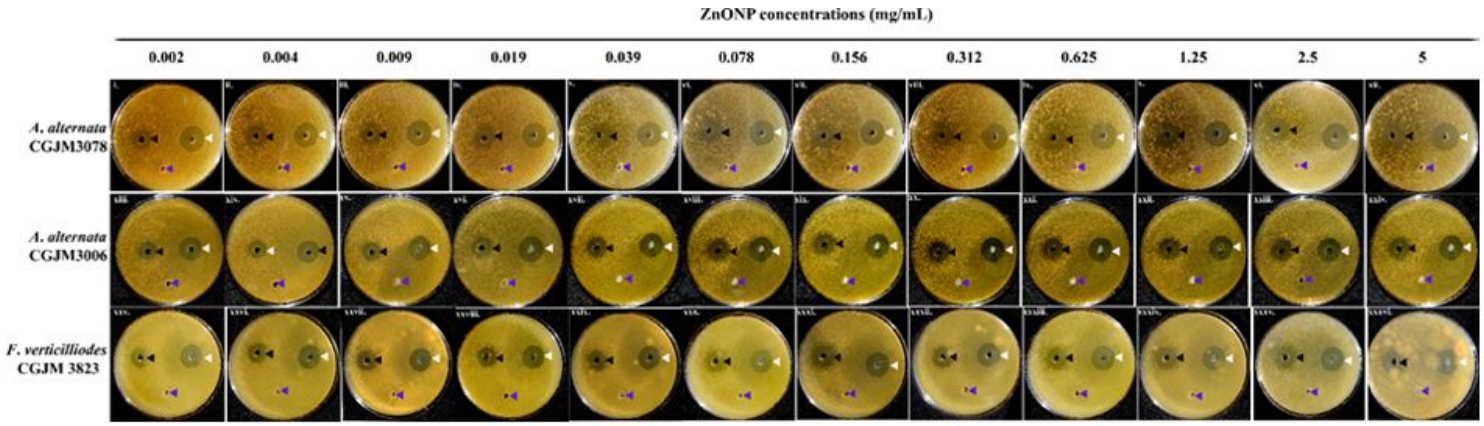

Figure 6

Plates representing the inhibition zones across a concentration range of ZnONPs against the fungal strains Alternaria alternata CGJM3078 (i– xii), A. alternata CGJM3006 (xiii – xxiv) and Fusarium verticilliodes CGJM 3823 (xxv-xxxvi). Black arrow heads indicate antimicrobial activities caused by ZnONPs, white indicates the bleach positive control, and blue indicates the sterile distilled w

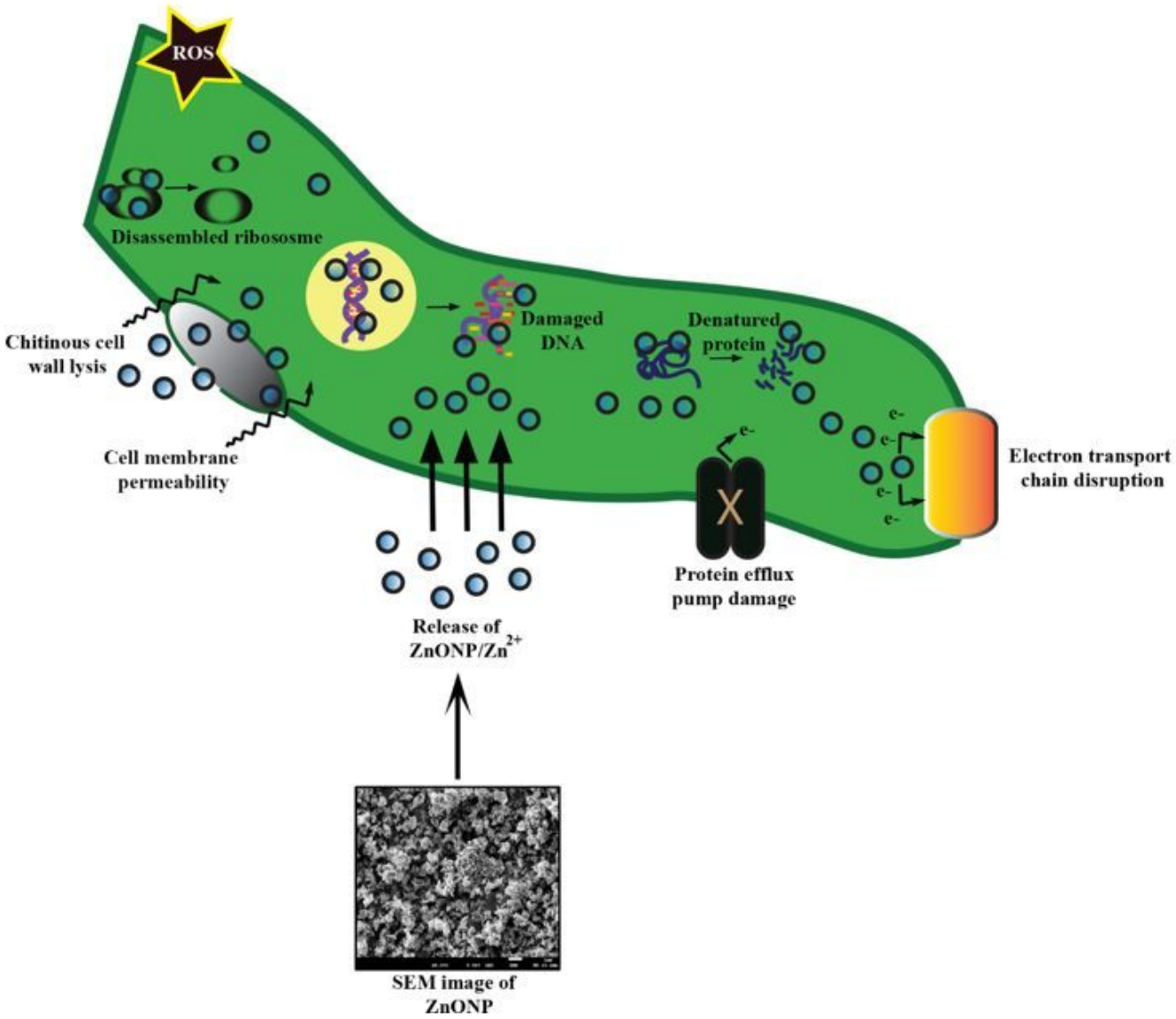

Figure 7

Schematic representation of the possible mechanism causing the antifungal ability of ZnONPs on a single fungal cell.

Supplementary Files

This is a list of supplementary files associated with this preprint. Click to download.

- ZnONPBPBFungalsupplementarymaterial.docx